Hexagonal Boron Nitride Single Crystal Growth from Solution with a Temperature Gradient

Jiahan Li, Yuan Chao, Christine Elias, Junyong Wang, Xiaotiang Zhang, Gaihua Ye, Huang Chaoran, Martin Kuball, Goki Eda, Joan M. Redwing, et al.

Hexagonal Boron Nitride Single Crystal Growth from Solution with a Temperature Gradient

*Jiahan Li, Chao Yuan, Christine Elias, Junyong Wang, Xiaotian Zhang, Gaihua Ye, Chaoran Huang, Martin Kuball, Goki Eda, Joan M. Redwing, Rui He, Guillaume Cassabois, Bernard Gil, Pierre Valvin, Thomas Pelini, Bin Liu and James H. Edgar**

Dr. J. Li, C. Huang, Prof. B. Liu, Prof. J. Edgar

Tim Taylor Department of Chemical Engineering, Kansas State University, Manhattan, Kansas 66506, USA

E-mail: edgarjh@ksu.edu

Dr. C. Yuan, Prof. M. Kuball,

Center for Device Thermography and Reliability (CDTR), H. H. Wills Physics Laboratory, University of Bristol, BS8 1TL Bristol, U.K

C. Elias, Prof. G. Cassabois, Prof. B. Gil, P. Valvin, Dr. T. Pelini

Laboratoire Charles Coulomb (L2C), Université de Montpellier, CNRS, Montpellier, 34095, France

Dr. J. Wang, Prof. Eda,

Department of Physics, National University of Singapore, 2 Science Drive 3, 117542, Singapore

Dr. X. Zhang, Prof. J. M. Redwing

Department of Materials Science and Engineering, 2D Crystal Consortium, Materials Innovation Platform, The Pennsylvania State University, University Park, Pennsylvania, 16802, USA

Gaihua Ye, Prof. Rui He

Department of Electrical and Computer Engineering, Texas Tech University, Lubbock, Texas 79409, USA

Abstract

Hexagonal boron nitride (hBN) is attracting much attention due to its tremendous applications including nanophotonic and electronic devices, substrates for two-dimensional (2D) materials, heat management materials, etc. To achieve the best device performance, large area hBN single crystals are required. Herein, large-area (>500 microns each), high-quality (defect density < $0.52/\mu m^2$) bulk hBN single crystals are grown from molten metal solutions with a temperature gradient. The narrow Raman linewidths of the intralayer E_{2g} mode peak and the interlayer shear mode, the strong and sharp phonon-assisted transition photoluminescence peaks, and the high thermal conductivity demonstrate that the hBN produced by this method are high crystal quality with a low density of defects. Atomic force microscope images show that atomically flat layers of hBN can be produced by exfoliation. This study not only demonstrates a new strategy for growing large hBN single crystals, but also provides high quality thick and thin hBN layers for nano device applications.

1. Introduction

Hexagonal boron nitride (hBN) has emerged as an essential material in a broad range of applications, including heat management of flexible nanoelectronics,[1, 2] electrically insulating substrates for other 2D materials,[3] hole-transport and electron-blocking layer in van der Waals heterostack LEDs,[4] infrared nanophotonics,[5, 6] single photon emitters,[7] flexible neutron detectors,[8, 9] deep UV emitters,[10] and membranes for hydrogen isotope separation.[11]

Structural defects such as grain boundaries, points defects and dislocations can alter hBN's electronic and optical properties, thus degrading the performance of hBN-containing devices.[12] To achieve the highest device performance possible, high-quality, large-area single crystal hBN is required.

We previously demonstrated high quality hBN crystal growth by the metal flux solution method with slow uniform cooling at atmospheric pressure.[13, 14] In this method, boron and nitrogen were dissolved at high temperature in a molten metal flux, then hBN crystals were precipitated as the solution is cooled. High-quality bulk hBN crystals were produced by both nickel/chromium[14] and iron/chromium fluxes.[15] The hBN grown from both solvents were of high-quality, as indicated by the narrow E_{2g} peak (a full-width-at-half-maximum (FWHM) of 8 cm^{-1})[14] in the Raman spectra and the presence of high energy peaks around 5.75 eV in the photoluminescence (PL) spectra.[16] In contrast, typically, the FWHM of the E_{2g} peak in the Raman spectra taken from chemical vapor deposition grown hBN is about 20- 30 cm^{-1},[17] and the high energy PL peaks are absent.[18, 19]

However, the slow cooling solution growth method has its limitations. Most significantly, the crystals precipitate over a wide range of temperatures, from the maximum temperature (1550 °C in our prior studies) until the flux completely solidifies (1350 °C or less).[13, 14] This is a problem

because the crystal quality and size tend to decrease as the temperature decreases.[20] To overcome these problems, in this work we induced large area bulk hBN single crystal growth by applying a temperature gradient across the molten metal flux. The source material dissolves in the high temperature region, and hBN crystals precipitate at the lower temperature region. The resulting crystal quality was characterized by Raman and photoluminescence spectroscopies and X-ray diffraction. The in-plane and out-of-plane thermal conductivities were measured by nanosecond transient thermoreflectance technology. Nanometer thick hBN layers were exfoliated from the bulk hBN flake and characterized by atomic force microscope and Raman mapping method.

2. Results and Discussion

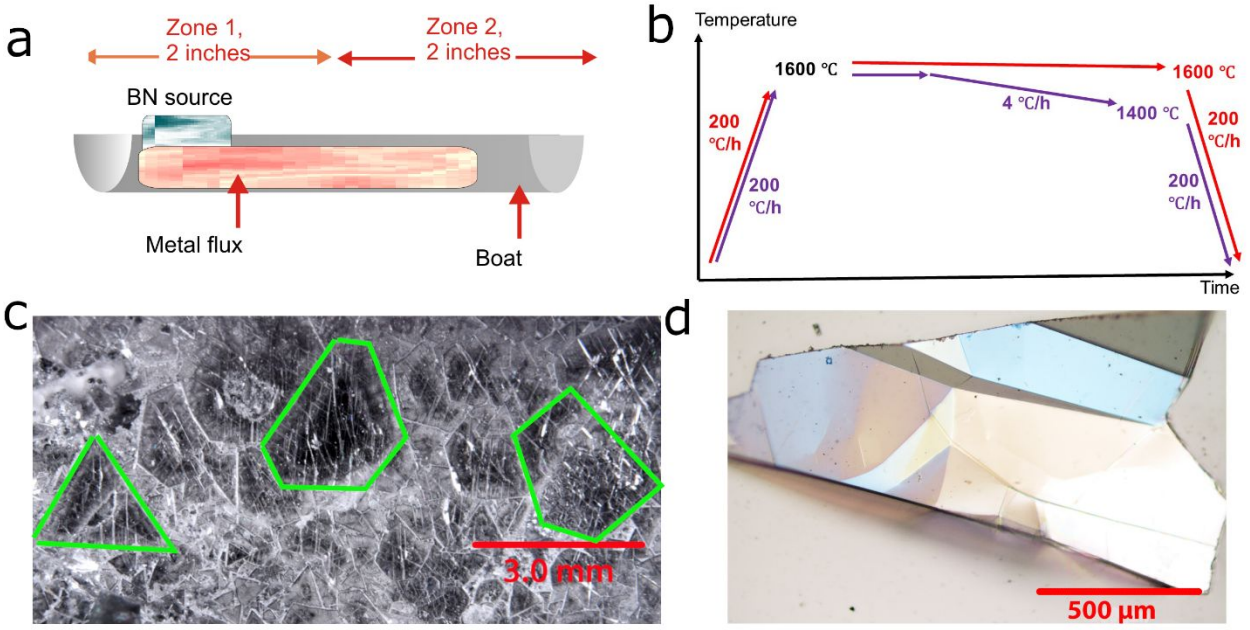

Figure 1. hBN bulk single crystal growth from metal flux with a temperature gradient. (a) Schematic diagram of the temperature gradient approach used for hBN crystal growth. (b)

Temperature profile for crystal growth. Furnace zone 1 was kept at 1600 ℃ during crystal growth process (red line) while zone 2 was cooled from 1600 ℃ to 1400 ℃ at a cooling rate of 4 ℃/h (purple line). (c) Macro image of the entire Fe-Cr ingot of zone 2 covered with hBN single crystals. Three crystal domains are outlined by a green line. (d) Micro images of hBN flake peeled from the ingot.

2.1 Crystal growth using temperature gradient technology

hBN single crystals were grown from a Cr-Fe flux using the temperature gradient technology (see the experimental section for details). A two-temperature zone furnace produced the temperature gradient, as shown in Figure 1a. Figure 1b illustrates the temperature profile for the two zones. During the hBN crystal precipitation process, the BN source dissolved continually in the high temperature zone (zone 1) and hBN crystals precipitated in the cooler zone (zone 2). hBN formed on zone 1 can be considered as the hBN produced by slow cooling. The morphology of crystal on zone 1 was nonuniform. The domain size was small (see supplementary section 1), presumably due to near uniform cooling and random nucleation. There exists a concentration gradient in the boat, as the temperature gradient drives boron and nitrogen transport through the solution from zone 1 to zone 2. In contrast, the morphology on zone 2 was uniform. The crystals zone 2 were clear and colorless.

After cooling to room temperature, hBN crystals covered the surface of Fe-Cr ingot. Figure 1c displays a macro images of hBN on the Cr-Fe ingot. In the area which was far away from boron nitride source, there were many hexagonal domains with sizes up to 3-4 mm (Figure 1c). As the process relies on random nucleation, [13, 14] it produces a multitude of relatively large (>500 microns) single crystals. Large-area hBN flakes were peeled from this area (Figure 1d). [20]

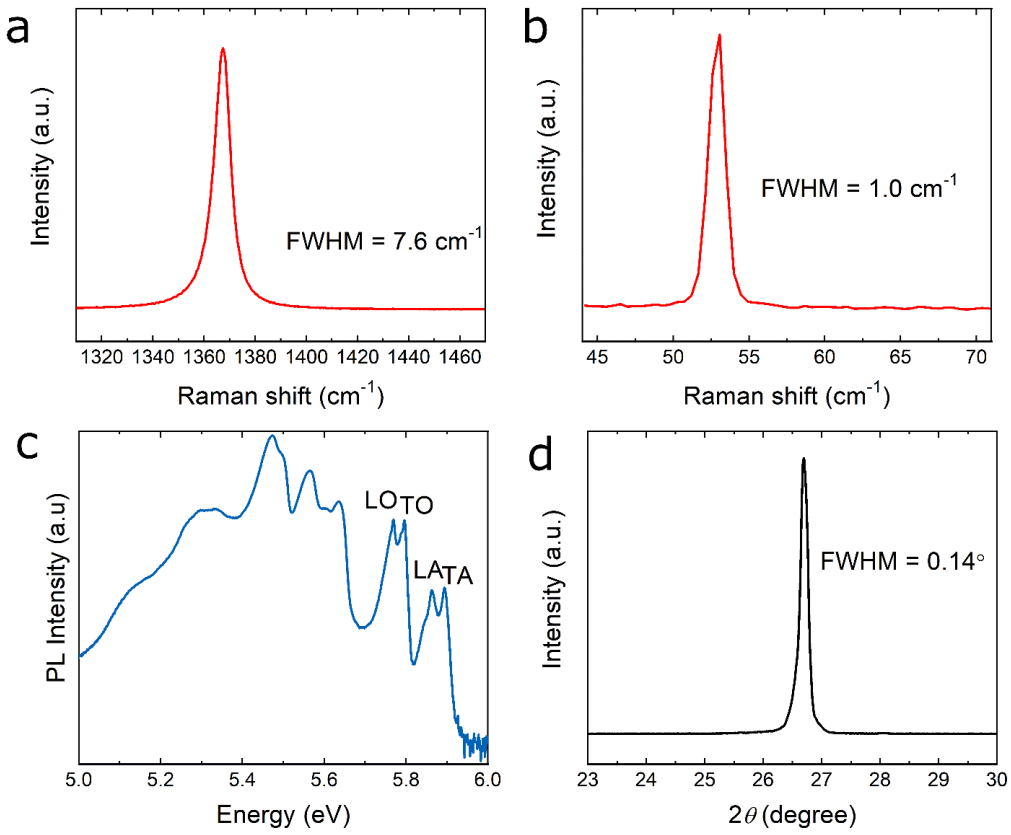

Figure 2. Characterization of hBN. Raman spectra from the (a) in-plane E_{2g} modes and (b) interlayer shear mode of a hBN flake. (c) Photoluminescence spectra of bulk hBN on a log scale at 8K ranging from 5 to 6 eV. PL spectra on a linear scale is shown in supplementary section 1. (d) X-ray diffraction pattern from the hBN.

2.2 Characterization of hBN

Figure 2a shows a Raman spectrum of the in-plane E_{2g} mode from hBN. This E_{2g} mode, which originates from the in-plane vibration between boron and nitrogen atoms, produces a peak at

1367.1 cm^{-1}. The FWHM of this E_{2g} mode is 7.6 cm^{-1}, which is similar to that from high-quality bulk hBN grown by slow cooling Fe-Cr flux (7.8 cm^{-1}),[13] indicating that our hBN is highly crystalline in-plane. The low-frequency Raman peak at 52.8 cm^{-1} (shown in Fig. 2b) corresponding to the rigid shear motion between adjacent layers has a FWHM of 1.0 cm^{-1}, comparable to that reported for high quality bulk hBN.[21] The presence of the interlayer shear mode and its narrow linewidth indicate that our hBN is highly crystalline in the c-direction.

Figure 2c displays the PL spectrum of hBN flake on a log scale at 8 K. As BN is an indirect bandgap semiconductor, during photon emission or absorption process, phonon emission/absorption is necessary to conserve momentum.[22] Therefore, the presence of phonon-assisted emission peaks between 5.7 and 6.0 eV in the spectra are indicative of high quality hBN single crystals.[23, 24] There are four phonon replicas (LO, TO, LA and TA) between 5.7 and 6.0 eV (Figure 2c), which indicates that the crystals are highly crystalline with a low defect density, and are comparable to bulk hBN grown by the slowly cooling solution method[16]. Moreover, the broad emission band below 5.7 eV (with peaks at 5.62, 5.56, 5.47 and 5.3 eV) has been identified as stacking fault defects-related emission in bulk hBN.[25] The peaks come from phonon-assisted inter-K valley scattering, which becomes observable because stacking defects in bulk hBN provide a density of final electronic states.[22] There are no peaks located around 4 eV, indicating a low concentration of point defects and impurities in this crystals. (see supplementary section 2).[26]

Figure 2d shows the XRD pattern of the hBN fake. The peak is centered at two theta equals 26.7° corresponding to diffraction by the (002) plane.[27] The FWHM is 0.14°, which is narrower than typical of hBN films produced by chemical vapor deposition or grown from metal solutions produced by slow cooling (0.6-0.3°).[14] The small FWHM also indicates highly crystalline hBN.

X-ray photoelectron spectroscopy shows that the binding energies for B_{1s} and N_{1s} are 190.3 eV and 397.8 eV (see supplementary section 3), respectively, which are comparable with previously reported values.[28]

To further investigate hBN defect density, we performed defect-controlled epitaxial growth of WSe_2 on our hBN (see supplementary section 4). We carried out the same multistep growth of WSe_2 as with the previous study[29] and estimated the nucleation density by counting the small triangular domains divided by area to determine the nucleation density after the nucleation step. The nucleation density of the WSe_2 is dictated by the point defects in the hBN point.[29] The nucleation density of WSe_2 on hBN was 0.52/μm^2. In a previous study, WSe_2 was deposited on mechanically exfoliated hBN, the nucleation density was 2.8/μm^2.[29] In our study, the nucleation density was 1/5 as much, indicating our hBN had a low defect density.

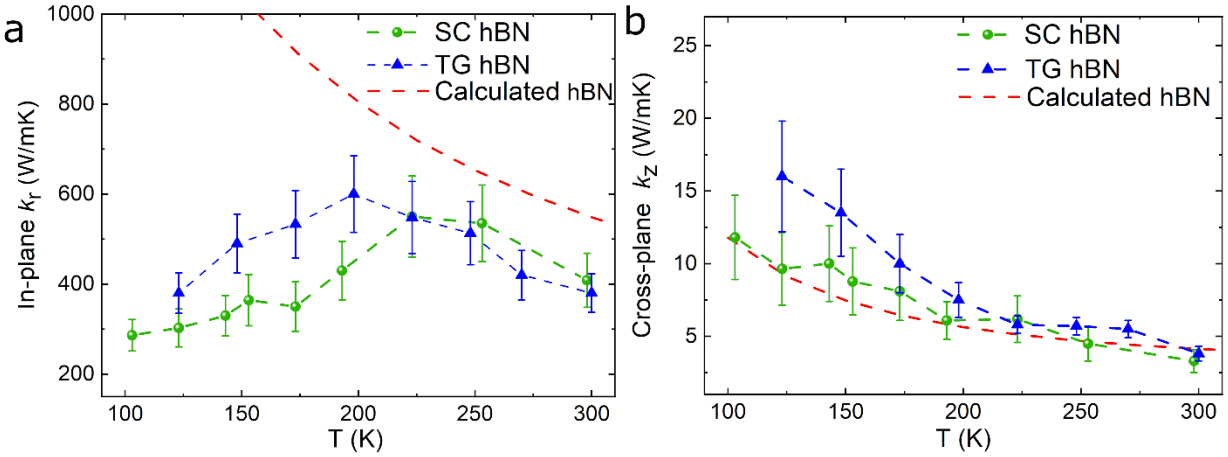

Figure 3. Temperature-dependent thermal conductivity of a hBN flake grown by the temperature gradient method. (a) In-plane (k_r) and (b) cross plane (k_z) of hBN flake (TG hBN, blue triangular), along with measurements on a hBN flake grown by slow cooling (SC hBN, green circle) and

theoretical results (red dash) from Boltzmann transport equation /density functional theory calculations.[30]

2.3 Temperature-dependent thermal conductivity of hBN flake

In semiconductor material, heat is mainly conducted by phonons, so thermal resistance is produced by intrinsic phonon-phonon, isotopic disorder, and extrinsic defects scattering.[31] At low temperature region where intrinsic phonon-phonon scattering is weak, thermal conductivity results are very sensitivity to the extrinsic scattering by crystal defects such as point defects (impurities and vacancies), grain boundary, dislocation, etc.[32-35] Thus, thermal conductivity measurements at low temperature can be used to characterize crystal quality, as shown in pyrolytic BN,[32] graphene,[36] carbon fiber,[37] and aluminum nitride.[38]

The in-plane (k_r) and out-of-plane (k_z) thermal conductivities of the hBN were measured by nanosecond transient thermoreflectance technology.[30, 39] In this technique, a 355 nm laser with a pulse duration of 10 ns and a spot size of 41 um is used as a heating pulse to induce a rapid temperature rise at the surface of Au transducer deposited at h-BN, and a continuous wave (CW), 532 nm laser is used to monitor the change in surface reflectance, and therefore temperature rise. An analytical photothermal pulses-induced thermal transport model was then used to analyze the measured temperature transients to obtain the thermal conductivity. A laser spot of 41 um initially heats on the surface, considering the lateral heat spreading in hBN, a volume with a lateral dimension up to 0.4 mm (estimated by the analytical thermal transport model) has been characterized with this technique. This large scanned volume could embrace all the local defects present in the materials, thus enabling the effective quantification of defects in hBN. Figure 3 compares the temperature dependent thermal conductivity of k_r and k_z for a hBN flake produced

by the temperature gradient method (TG-hBN) from the current study, with a hBN flake produced by slow cooling (SC-hBN) and theoretical calculation results.[30]The intrinsic isotopic and phonon-phonon scatterings mostly affect the thermal conductivity from intermediate to room and higher temperature, while the defects scattering mostly affect the thermal conductivity at low temperature. In the temperature ranging from 125 K to 200 K, TG-hBN and SC-hBN crystals have the exact same intrinsic isotopic and phonon-phonon scattering, so the higher k_r of the TG-hBN flake (blue triangular) (Figure 3a) originates from a lower extrinsic defect density than the SC-hBN. Between 200 K to 300 K, the intrinsic isotopic and phonon-phonon scatterings dominate heat transfer, considering the uncertainty,[30] so the k_r values are comparable between TG-hBN and SC-hBN. At room temperature, k_r was 380 ± 43 $Wm^{-1}K^{-1}$, which is consistent with reported values of natural hBN. [30, 32, 40]

As shown in figure 3b, the k_z (blue triangular) of the hBN crystal grown in this study was significantly higher than hBN produced by the slow cooling method (green curve) between 100K and 200K. This result, along with the Raman and XRD results (the small FWHM of shear mode Raman vibration and 2θ peak at XRD) confirm that the quality of the hBN produced in this study is higher quality than the hBN grown by slow cooling. At room temperature, the k_z was 4.3 ± 0.6 $W\ m^{-1}\ K^{-1}$, which is also in good agreement with the literature values.[30, 40]

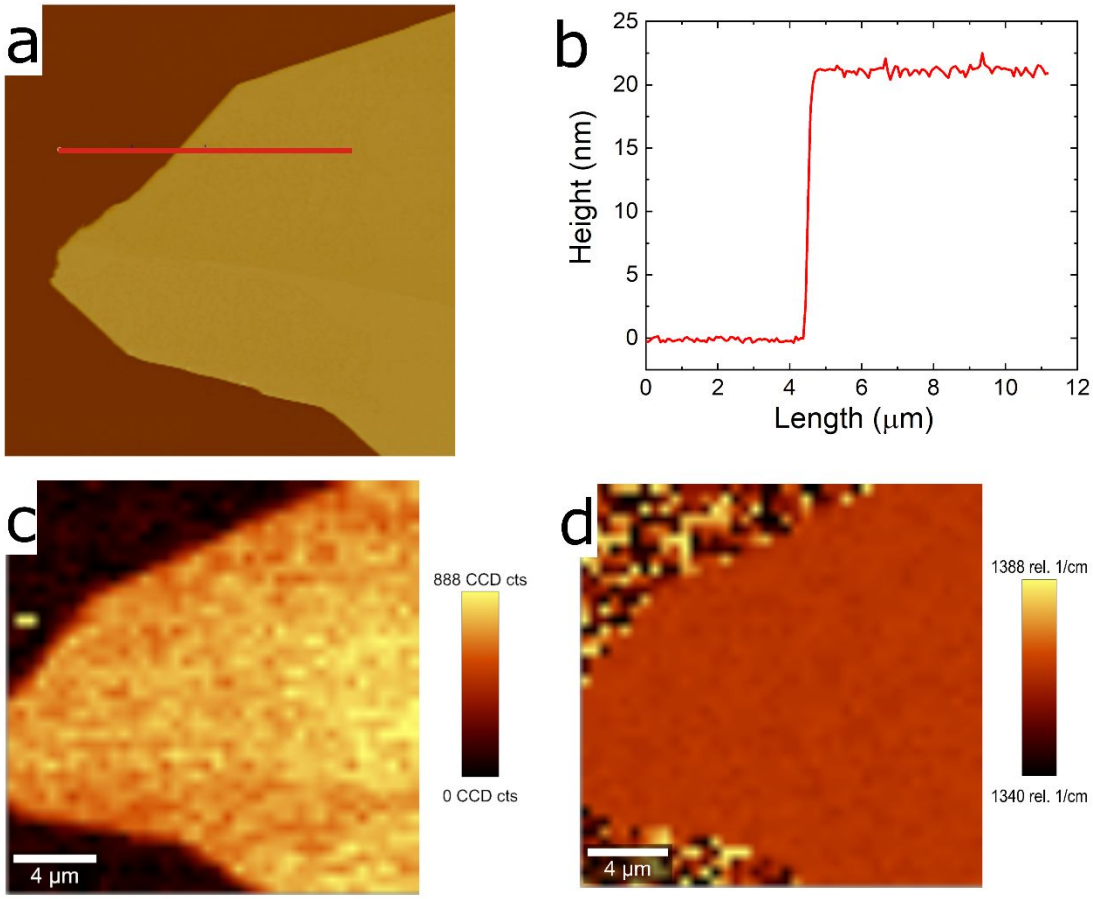

Figure 4. Characterization of an exfoliated hBN sheet. (a) AFM image of an exfoliated hBN sheet on a substrate. (b) The height profile of the exfoliated hBN sheet along the line in (a). (c) Raman intensity map of E_{2g} peak. (d) Raman position map of the E_{2g} peak.

2.4 Exfoliated hBN sheet

For device fabrication, thin, nanometer thick hBN layers are needed, and these must be exfoliated from the bulk hBN flake. To demonstrate the potential of our hBN for nano device applications, hBN nanolayers were produced by mechanical exfoliation. Figure 4a shows an AFM image of an exfoliated hBN film. It was 20 nm thick (Figure 4b). Figure 4c and 4d show Raman mapping image

of the E_{2g} peak. As shown in Figure 4c, the Raman intensity did not change over the entire flake, suggesting it had a uniform thickness. The Raman peak position was consistent everywhere (Figure 4d), indicating that the hBN nanolayer is highly crystalline on all surface. The high-quality of our hBN film implies that our hBN is a good candidate for device applications such as a substrate for 2D layers, tunnel barriers or encapsulation layers.

3. Conclusion

Large-area and few-defect hBN single crystals were grown using the metal flux method with a temperature gradient to drive crystal growth. Using this method, the maximum crystal domain size demonstrated was 4 mm. The narrow linewidth of Raman modes (FWHM of 7.6 cm^{-1} and 1 cm^{-1} for in-plane and shear modes, respectively) and the presence of the intrinsic phonon-assisted emission peaks in the photoluminescence spectra indicate that our hBN is highly crystalline. The narrow XRD peak demonstrates that our hBN has few stacking defects. In addition, in-plane thermal conductivity measurements confirm that our hBN flake has few defects density within the large area at in-plane directions. High cross-plane thermal conductivity is evidence that this hBN is also highly ordered in the *c*-direction. Moreover, highly crystalline hBN nanolayers were prepared by mechanical exfoliation. AFM and Raman map characterization show our hBN has that a uniform and atomically smooth surface, which suggests that the hBN film is of great potential for nanodevice application. The work not only inspires a new strategy for large single crystal growth but also provides a high-quality hBN flake and film for nano device applications.

4. Experimental Section

Crystal growth and hBN flake preparation： A two zone horizontal alumina tube furnace was used to grow hBN crystals. The source material was a piece of hot-pressed boron nitride placed in the hot end of the alumina boat while the metal was uniformly distributed throughout (Figure 1a). Boron and nitrogen were dissolved into a 50wt% Fe-50wt% Cr metal flux.[13] Before heating the furnace, the tube was purged three time with nitrogen and forming gas (H_2 5% and Ar 95%). During the heating process, nitrogen and forming gas flowed through the furnace system at rates of 5 SLM and 20 SCCM, respectively. Two heating zones were applied to produce the temperature gradient. The boat was located at in the center line of the two furnace zones. Figure 1b show the temperature profile of the two zones. At beginning of experiment, both zone 1 and 2 were heated to 1,600 ℃ for 24h to dissolve the boron and nitrogen. During crystal growth process, zone 1 was held at 1,600 ℃ while zone 2 was cooled rate of 4℃ /h to 1400 °C, thus a temperature gradient was formed between heating zone 1 and 2. Crystal formed during zone 2 cooling process. Finally, two zones were quenched to room temperature to form Fe-Cr ingot. hBN crystals covered Fe-Cr ingot surface. hBN flakes were peeled from the Fe-Cr ingot using thermal release tape. The tape was heated at 130 ℃ then washed by acetone, to release the hBN flakes.

Photoluminescence spectroscopy： The samples were held on the cold finger of a closed-cycle cryostat at a temperature of 10K. The excitation beam is the fourth harmonic of a cw mode-locked Ti-Sa oscillator (194 nm) with a repetition frequency of 82 MHz. The beam is focused on the sample with a spot diameter of ~50μm and a power of ~35μW. An achromatic optical system couples the emitted signal to our detection system using parabolic mirrors with a special coating

for deep UV. The detection system is composed of a f=300mm Czerny-Turner monochromator, equipped with a 1800 grooves/mm grating blazed at 250 nm, and a back-illuminated CCD camera (Andor Newton 920), with a quantum efficiency of 50% at 210 nm, operated over integration times of 1 min.

Raman spectra: Raman characterization was performed at room temperature using a Horiba Labram HR Raman microscope system. A 532 nm laser with power less than 0.6 mW was used. The laser was focused by a 100× lens to a spot diameter of ~1 μm. Using an 1800 groove/mm grating, we achieved a spectral resolution of ~0.5 cm^{-1}.

X-ray diffraction: hBN flakes were stacked and covered the entire Si/SiO_2 substrate. A Cu K-alpha source was used.

Thermal conductivity measurement: A transient thermoreflectance technique was applied to measure both the out-of-plane and in-plane thermal conductivity of hBN.[30, 39] Briefly, a 50 nm Au film was deposited on hBN flake surface as transducer, with a 10 nm Ti interlayer for good adhesion. A 10 ns, 355 nm pulsed pump laser heated the Au film to produce a temperature response. The temperature response was determined by the change in the intensity of a 532 nm laser reflected from the Au film. The sample temperature was controlled by a from 100 K to 300 K. The measured transients were analyzed with a photothermal pulses-induced thermal transport model.[30] The measured normalized transients overlapped with the model fitting are shown at section in supplementary section 5.

Supporting Information

Supporting Information is available on the ACS Publications website, including optical micrograph of hBN crystals on zone 1 and zone 2, PL spectrum of hBN flake on a linear scale at 8 K, X-Ray photoelectron spectroscopy of hBN, epitaxial growth of WSe_2 on hBN and the best fit of our model results to an example measured transient.

Acknowledgements

The crystal growth (J.L. and J.H.E) in this study was supported by the Materials Engineering and Processing program of the National Science Foundation, Award Number CMMI 1538127. C. H. and B. L. are grateful for the support by NSF grant CHE-1726332. J. W. and G. E. acknowledges the Singapore National Research Foundation for funding the research under medium-sized centre programme. G.E. also acknowledges support from the Ministry of Education (MOE), Singapore, under AcRF Tier 3 (MOE2018-T3-1-005). X. Z. and J.M.R. acknowledge the support of National Science Foundation (NSF) through the 2D Crystal Consortium-Materials Innovation Platform (2DCC-MIP) under NSF cooperative agreement DMR-1539916. Work at Texas Tech University (G. Y. and R. H.) is supported by NSF CAREER Grant (No. DMR-1760668).

References

(1) Akinwande, D., Petrone, N.; Hone, J. Two-dimensional flexible nanoelectronics. *Nature communications* **2014,** *5,* 5678.

(2) Cai, Q., Scullion, D., Gan, W., Falin, A., Zhang, S., Watanabe, K., Taniguchi, T., Chen, Y., Santos, E. J.; Li, L. H. High thermal conductivity of high-quality monolayer boron nitride and its thermal expansion. *Science advances* **2019,** *5,* eaav0129.

(3) Zhang, Z., Hu, S., Chen, J.; Li, B. Hexagonal boron nitride: a promising substrate for graphene with high heat dissipation. *Nanotechnology* **2017,** *28,* 225704.

(4) Wang, S., Wang, J., Zhao, W., Giustiniano, F., Chu, L., Verzhbitskiy, I., Zhou Yong, J.; Eda, G. Efficient carrier-to-exciton conversion in field emission tunnel diodes based on MIS-type van der Waals heterostack. *Nano letters* **2017,** *17,* 5156.

(5) Dai, S., Tymchenko, M., Yang, Y., Ma, Q., Pita-Vidal, M., Watanabe, K., Taniguchi, T., Jarillo-Herrero, P., Fogler, M. M.; Alù, A. Manipulation and steering of hyperbolic surface polaritons in hexagonal boron nitride. *Adv Mater* **2018,** *30,* 1706358.

(6) Caldwell, J. D., Kretinin, A. V., Chen, Y., Giannini, V., Fogler, M. M., Francescato, Y., Ellis, C. T., Tischler, J. G., Woods, C. R.; Giles, A. J. Sub-diffractional volume-confined polaritons in the natural hyperbolic material hexagonal boron nitride. *Nature communications* **2014,** *5,* 5221.

(7) Nguyen, M., Kim, S., Tran, T. T., Xu, Z., Kianinia, M., Toth, M.; Aharonovich, I. Nanoassembly of quantum emitters in hexagonal boron nitride and gold nanospheres. *Nanoscale* **2018,** *10,* 2267.

(8) Maity, A., Grenadier, S., Li, J., Lin, J.; Jiang, H. Toward achieving flexible and high sensitivity hexagonal boron nitride neutron detectors. *Appl. Phys. Lett.* **2017,** *111,* 033507.

(9) Maity, A., Doan, T., Li, J., Lin, J.; Jiang, H. Realization of highly efficient hexagonal boron nitride neutron detectors. *Appl. Phys. Lett.* **2016,** *109,* 072101.

(10) Vuong, T., Cassabois, G., Valvin, P., Rousseau, E., Summerfield, A., Mellor, C., Cho, Y., Cheng, T., Albar, J. D.; Eaves, L. Deep ultraviolet emission in hexagonal boron nitride grown by high-temperature molecular beam epitaxy. *2D Materials* **2017,** *4,* 021023.

(11) Lozada-Hidalgo, M., Hu, S., Marshall, O., Mishchenko, A., Grigorenko, A. N., Dryfe, R. A., Radha, B., Grigorieva, I. V.; Geim, A. K. Sieving hydrogen isotopes through two-dimensional crystals. *Science* **2016,** *351,* 68.

(12) Rasool, H. I., Ophus, C.; Zettl, A. Atomic defects in two dimensional materials. *Adv Mater* **2015,** *27,* 5771.

(13) Liu, S., He, R., Ye, Z., Du, X., Lin, J., Jiang, H., Liu, B.; Edgar, J. H. Large-Scale Growth of High-Quality Hexagonal Boron Nitride Crystals at Atmospheric Pressure from an Fe–Cr Flux. *Crystal Growth & Design* **2017,** *17,* 4932.

(14) Hoffman, T. B., Clubine, B., Zhang, Y., Snow, K.; Edgar, J. H. Optimization of Ni–Cr flux growth for hexagonal boron nitride single crystals. *J. Cryst. Growth* **2014,** *393,* 114.

(15) Song, L., Ci, L., Lu, H., Sorokin, P. B., Jin, C., Ni, J., Kvashnin, A. G., Kvashnin, D. G., Lou, J.; Yakobson, B. I. Large scale growth and characterization of atomic hexagonal boron nitride layers. *Nano letters* **2010,** *10,* 3209.

(16) Vuong, T., Liu, S., Van der Lee, A., Cuscó, R., Artús, L., Michel, T., Valvin, P., Edgar, J., Cassabois, G.; Gil, B. Isotope engineering of van der Waals interactions in hexagonal boron nitride. *Nature materials* **2018,** *17,* 152.

(17) Dahal, R., Ahmed, K., Wu, J. W., Weltz, A., Lu, J. J., Danon, Y.; Bhat, I. B. Anisotropic charge carrier transport in free-standing hexagonal boron nitride thin films. *Applied Physics Express* **2016,** *9,* 065801.

(18) Dahal, R., Li, J., Majety, S., Pantha, B., Cao, X., Lin, J.; Jiang, H. Epitaxially grown semiconducting hexagonal boron nitride as a deep ultraviolet photonic material. *Appl. Phys. Lett.* **2011,** *98,* 211110.

(19) Majety, S., Cao, X., Li, J., Dahal, R., Lin, J.; Jiang, H. Band-edge transitions in hexagonal boron nitride epilayers. *Appl. Phys. Lett.* **2012,** *101,* 051110.

(20) Bugaris, D. E.; zur Loye, H. Materials discovery by flux crystal growth: quaternary and higher order oxides. *Angewandte Chemie International Edition* **2012,** *51,* 3780.

(21) Liu, S., He, R., Xue, L., Li, J., Liu, B.; Edgar, J. H. Single Crystal Growth of Millimeter-Sized Monoisotopic Hexagonal Boron Nitride. *Chemistry of Materials* **2018,** *30,* 6222.

(22) Cassabois, G., Valvin, P.; Gil, B. Hexagonal boron nitride is an indirect bandgap semiconductor. *Nature Photonics* **2016,** *10*, 262**.**

(23) Cassabois, G., Valvin, P.; Gil, B. Intervalley scattering in hexagonal boron nitride. *Physical Review B* **2016,** *93,* 035207.

(24) Li, J., Cao, X., Hoffman, T. B., Edgar, J. H., Lin, J.; Jiang, H. Nature of exciton transitions in hexagonal boron nitride. *Appl. Phys. Lett.* **2016,** *108,* 122101.

(25) Vuong, T., Cassabois, G., Valvin, P., Jacques, V., Cuscó, R., Artús, L.; Gil, B. Overtones of interlayer shear modes in the phonon-assisted emission spectrum of hexagonal boron nitride. *Physical Review B* **2017,** *95,* 045207.

(26) Vuong, T., Cassabois, G., Valvin, P., Ouerghi, A., Chassagneux, Y., Voisin, C.; Gil, B. Phonon-photon mapping in a color center in hexagonal boron nitride. *Phys. Rev. Lett.* **2016,** *117,* 097402.

(27) Ahmed, K., Dahal, R., Weltz, A., Lu, J. J., Danon, Y.; Bhat, I. B. Effects of sapphire nitridation and growth temperature on the epitaxial growth of hexagonal boron nitride on sapphire. *Materials Research Express* **2017,** *4,* 015007.

(28) Zhang, C., Zhao, S., Jin, C., Koh, A. L., Zhou, Y., Xu, W., Li, Q., Xiong, Q., Peng, H.; Liu, Z. Direct growth of large-area graphene and boron nitride heterostructures by a co-segregation method. *Nature communications* **2015,** *6,* 6519.

(29) Zhang, X., Zhang, F., Wang, Y., Schulman, D. S., Zhang, T., Bansal, A., Alem, N., Das, S., Crespi, V. H.; Terrones, M. Defect-Controlled Nucleation and Orientation of WSe2 on hBN–A Route to Single Crystal Epitaxial Monolayers. *ACS nano* **2019,** *13*, 3341

(30) Yuan, C., Li, J., Lindsay, L., Cherns, D., Pomeroy, J. W., Liu, S., Edgar, J. H.; Kuball, M. Modulating the thermal conductivity in hexagonal boron nitride via controlled boron isotope concentration. *Communications Physics* **2019,** *2,* 43.

(31) Lindsay, L., Broido, D.; Reinecke, T. Phonon-isotope scattering and thermal conductivity in materials with a large isotope effect: A first-principles study. *Physical Review B* **2013,** *88,* 144306.

(32) Sichel, E., Miller, R., Abrahams, M.; Buiocchi, C. Heat capacity and thermal conductivity of hexagonal pyrolytic boron nitride. *Physical review B* **1976,** *13,* 4607.

(33) Polanco, C. A.; Lindsay, L. Thermal conductivity of InN with point defects from first principles. *Physical Review B* **2018,** *98,* 014306.

(34) Lindsay, L.; Broido, D. Enhanced thermal conductivity and isotope effect in single-layer hexagonal boron nitride. *Physical Review B* **2011,** *84,* 155421.

(35) Katre, A., Carrete, J., Dongre, B., Madsen, G. K.; Mingo, N. Exceptionally strong phonon scattering by B substitution in cubic SiC. *Phys. Rev. Lett.* **2017,** *119,* 075902.

(36) Kelly, B.; Gilchrist, K. The basal thermal conductivity of highly oriented pyrolytic graphite as a function of degree of graphitisation. *Carbon* **1969,** *7,* 355.

(37) Nysten, B., Issi, J., Barton Jr, R., Boyington, D.; Lavin, J. Determination of lattice defects in carbon fibers by means of thermal-conductivity measurements. *Physical Review B* **1991,** *44,* 2142.

(38) Cheng, Z., Koh, Y. R., Mamun, A., Shi, J., Bai, T., Huynh, K., Yates, L., Liu, Z., Li, R.; Lee, E. Experimental Observation of High Intrinsic Thermal Conductivity of AlN. *arXiv preprint arXiv:1911.01595* **2019,**

(39) Yuan, C., Waller, W. M.; Kuball, M. Nanosecond transient thermoreflectance method for characterizing anisotropic thermal conductivity. *Rev. Sci. Instrum.* **2019,** *90,* 114903.

(40) Jiang, P., Qian, X., Yang, R.; Lindsay, L. Anisotropic thermal transport in bulk hexagonal boron nitride. *Physical Review Materials* **2018,** *2,* 064005.

Table of Contents Graphic